Universiteit Leiden
The Netherlands

Computer-aided techniques for assessment of MRI-detected inflammation for early identification of inflammatory arthritis
Aizenberg, E.

Cover Page

Universiteit Leiden

Author: Aizenberg, E.
Title: Computer-aided techniques for assessment of MRI-detected inflammation for early identification of inflammatory arthritis
Issue Date: 2019-03-14

3

Automatic quantification of bone marrow edema on MRI of the wrist in patients with early arthritis

Abstract

Purpose: To investigate the feasibility of automatic quantification of bone marrow edema (BME) on MRI of the wrist in patients with early arthritis.

Methods: For 485 early arthritis patients (clinically confirmed arthritis of ≥ 1 joint, symptoms for < 2 years), MR scans of the wrist were processed in three automatic stages. First, super-resolution reconstruction was applied to fuse coronal and axial scans into a single high-resolution three-dimensional image. Next, the carpal bones were located and delineated using atlas-based segmentation. Finally, the extent of BME within each bone was quantified by identifying image intensity values characteristic of BME by fuzzy clustering and measuring the fraction of voxels with these characteristic intensities within each bone. Correlation with visual BME scores was assessed through Pearson correlation coefficient.

Results: Pearson correlation between quantitative and visual BME scores across 485 patients was $r = 0.83$, $P < 0.001$.

Conclusion: Quantitative measurement of BME on MRI of the wrist has potential to provide a feasible alternative to visual scoring. Complete automation requires automatic detection and compensation of acquisition artifacts.

Introduction

The presence of bone marrow edema-like abnormalities (BME) has been shown to be a strong predictor of radiographic progression in rheumatoid arthritis (RA) patients [1–4], and is therefore an important biomarker in early arthritis. Evaluation of BME is done on MRI, where it is visually scored based on the Outcome Measures in Rheumatology RA-MRI Scoring (RAMRIS) system [5,6]. This scoring method requires a trained reader to visually estimate the volume of BME. Such estimates are challenging and time-consuming because of the need to assess multiple imaging planes and slices and are inherently undermined by the simultaneous contrast effect [7–9] of the human visual system, which causes the reader to perceive the same image intensity value differently depending on surrounding background intensities.

An automatic and quantitative approach to evaluating BME on MR scans could overcome the limitations of visual scoring by offering high-precision measurements derived directly from three-dimensional (3D) image data. It could alleviate the time burden of training and manual scoring for clinical researchers and could facilitate the use of MRI in drug evaluation studies, where employing a trained team of readers is costly.

Several previous studies on BME quantification in the wrist joint [10–12] relied on a semi-automatic method proposed by Li *et al.* [13]. However, this technique requires an expert to manually delineate non-edema and edema regions of interest within every bone that needs to be evaluated. These studies were also limited to a small sample size of fewer than 20 subjects. One related study focuses on fully automatic BME quantification in the knee joint [14], but it is not directly clear how to extend the bone segmentation method [15] to a joint with more than two bones, as is the case in the wrist.

In the work presented here, we developed an automatic framework for measuring the fraction of bone volume affected by BME in the eight carpal bones of the wrist joint. In contrast to previous methods, we used atlas-based segmentation to automatically locate and delineate the carpal bones. Our aim was

to investigate the feasibility of BME quantification through such atlas-based approach and assess the correlation between quantitative measurements and visual BME scores in a large cohort of early arthritis patients.

Methods

Patients

A total of 573 early arthritis patients from the Leiden Early Arthritis Clinic (EAC) cohort [16] (mean age, 54.7 years; age range, 18.1–87.9 years) were studied: 354 female (mean age, 53.0 years; age range, 18.7–85.3 years) and 219 male (mean age, 57.5 years; age range, 18.1–87.9 years) patients. Inclusion required clinically confirmed arthritis by physical examination in $\geq$ 1 joint and symptom duration of < 2 years. MR scans were obtained for the wrist joint of the most painful side (or the dominant side in cases of equally severe symptoms on both sides). The study was approved by the institutional medical ethics committee and all participants provided written informed consent.

MRI sequences

The wrist joint was scanned with an ONI MSK Extreme 1.5T extremity MR scanner (GE, Wisconsin, USA) with a 100 mm coil. Before contrast agent injection, T1-weighted fast spin-echo (FSE) sequence (T1) was acquired in the coronal plane with repetition time (TR) of 650 ms, echo time (TE) of 17 ms, acquisition matrix 388×288, echo train length (ETL) 2. After intravenous injection of Gd-chelate (gadoteric acid, Guerbet, Paris, France, standard dose of 0.1 mmol/kg), T1-weighted FSE sequence with frequency-selective fat saturation (T1-Gd) was obtained in the coronal plane (TR 650/TE 17, acquisition matrix 364×224, ETL 2) and the axial plane (TR 570/TE 7, acquisition matrix 320×192, ETL 2). Coronal sequences were acquired with a slice thickness of 2 mm and a slice gap of 0.2 mm. Axial sequences were acquired with a slice thickness of 3 mm and a slice gap of 0.3 mm. The use of a T1-Gd sequence instead of a T2-weighted fat-saturated sequence is a validated modification that has been shown to perform

equally well in the depiction of BME and allows for a faster scanning protocol [17,18], which in turn reduces patient discomfort. Safety risk was minimized to the degree possible by the use of a macrocyclic contrast agent [19,20].

Visual scoring of BME

BME was assessed in line with the definitions proposed by RAMRIS [5] with validated modification of substituting T2-weighted fat-saturated sequence with T1-Gd sequence [17,18]. BME was independently scored by two trained readers who were blinded to clinical data on a 0–3 scale based on the estimated fraction of affected bone volume: 0, no BME; 1, 1–33% of bone edematous; 2, 34–66%; 3, 67–100%. The within-reader intra-class correlation coefficients (ICCs) for the total inflammation score were 0.98 and 0.93; the between-reader ICC was 0.95. The mean BME score of the two readers was considered.

Patients for which at least one reader marked one or more bones as unscorable (typically due to fat suppression issues) were excluded ($n =11$). Patients whose T1-Gd images suffered from incomplete fat suppression, but still considered scorable by readers based on T1 images showing low signal intensity in the matching areas with BME on T1-Gd were retained.

Quantitative image analysis framework

Our automatic framework consisted of three stages. First, super-resolution reconstruction was applied to fuse coronal and axial T1-Gd scans into a single high-resolution 3D image. Next, the carpal bones were located and delineated using atlas-based segmentation. Finally, the extent of BME within each bone was quantified by identifying image intensity values characteristic of BME by fuzzy clustering and measuring the fraction of voxels with these characteristic intensities within each bone. Note that since the super-resolution reconstruction step requires a coronal and axial scan of the same sequence as input, this stage, and therefore the entire framework, could only be applied to T1-Gd scans. Therefore, pre-contrast T1

images, which were acquired only in the coronal plane, were not used in the quantitative image analysis framework.

Super-resolution reconstruction

When readers evaluate BME visually, they make use of two complementary scans: one acquired in the coronal plane and the second in the axial plane. This is due to the fact that slice thickness in each of the scans (2 mm in coronal; 3 mm in axial) is much larger than the in-plane spacing between voxels (~0.2 mm). Therefore, one scan compensates for anatomical detail lost in the other scan, allowing the reader to perceptually form a more complete assessment of the anatomy. Naturally, this raises the question how to simulate such perceptual fusion of two images on the computer, in order to obtain a single 3D image with isotropic voxels and high resolution in all three viewing planes. This type of problem, reconstruction of a high-resolution image of an object from multiple low-resolution images of the same object, is commonly referred to as super-resolution reconstruction (SRR).

A variety of SRR methods have been proposed for MRI [21–24]. In this study, we applied the method developed by Poot *et al.* [24]. This algorithm belongs to the family of spatial domain SRR methods, which construct a linear model of the image acquisition system and reconstruct the high-resolution image by solving a system of linear equations. This system is often underdetermined, as in our case, and is solved by applying regularization. We used Laplacian regularization with parameter $\lambda = 0.05$. This value was optimized in an experiment by two expert radiologists (MR and JLB) to provide satisfactory balance between image noise/artifacts and visual clarity of BME, synovial tissue, cartilage, and fluid around tendons. Prior to applying SRR, the axial scan was spatially aligned to the coronal scan using the Elastix software package [25,26], axial image intensity was linearly matched to the coronal image intensity, and the field of view of both images was restricted to the overlapping physical space between the two scans. Figure 1 shows an example of applying SRR to a pair of coronal and axial scans.
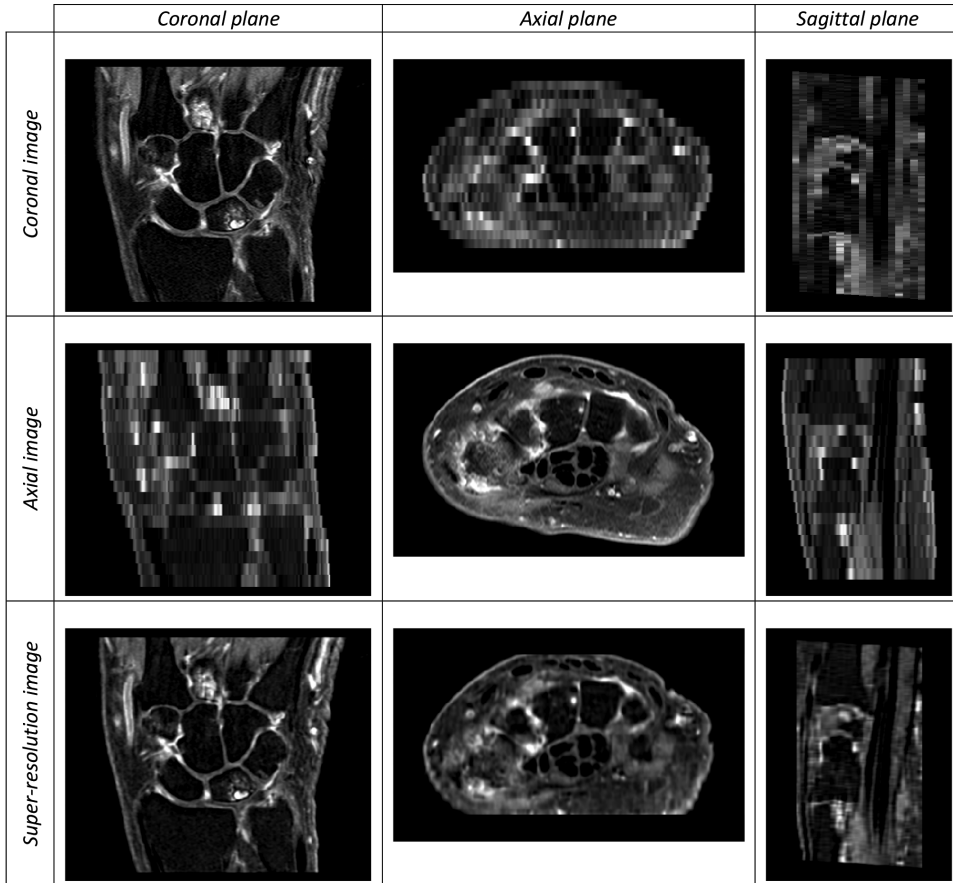
Figure 1. Coronal, axial, and super-resolution images (top to bottom rows, respectively) and their coronal, axial, and sagittal viewing planes (left to right columns, respectively). The original scans exhibit high resolution only in one plane, while the super-resolution image exhibits high resolution in all three planes.

Segmentation of carpal bones

The carpal bones were located and delineated using atlas-based segmentation (ABS) [27]. The atlas consisted of 13 early arthritis patients. For each atlas patient, the carpal bones were manually segmented in the coronal and axial T1-Gd images, yielding two segmentation images. The voxels of these manual segmentation images were assigned an integer bone label value ranging from 1 to 8 in locations corresponding to one of the eight carpal bones, or otherwise the value 0 in locations outside the bones. Then, separately for each bone, the two manual segmentation images were fused using SRR. Voxels with values above 78% of the

bone label value were assigned the bone label value, and the remaining voxels were zeroed to discard noise. The resulting eight images were superimposed to obtain the complete segmentation image in high-resolution space.

The first phase of the ABS routine consisted of image registration between each of the 13 atlas images and the target image being segmented. Image registration (using Elastix [25]) was done in two stages [28]: first, a similarity mapping to account for global translation, rotation, and scaling, followed by a B-spline mapping to account for local deformations. After spatially mapping carpal bone segmentations from every atlas image onto the target image, a majority vote was applied across all mappings, determining whether a voxel was labeled as background or as one of the carpal bones.

It should be noted that all atlas images contained the right wrist joint. For segmentation of the left wrist, atlas images were horizontally mirrored prior to registration. In order to avoid biased measurements, patients that were part of the ABS atlas were excluded from optimization and validation phases.

Assessment of segmentation accuracy

To assess the accuracy of ABS, a leave-one-out cross-validation was performed. In each of the 13 runs, 12 out of 13 atlas images would constitute the atlas set, and the remaining image would be used as the target image to be segmented. The result was validated against manual segmentation of the coronal T1-Gd image. Segmentation accuracy was evaluated by computing precision and recall rates for each carpal bone. Here, precision rate refers to the fraction of voxels segmented by ABS that overlap with the manual bone segmentation, while recall rate refers to the fraction of voxels within the manual bone segmentation that were correctly segmented by ABS.

BME quantification

BME is characterized by high signal intensity on T1-Gd images due to contrast enhancement and the suppressed normal fatty bone marrow. The precise intensity values vary per acquisition, depending on the strength of contrast enhancement and

fat suppression. The variation of these values is further broadened by inherent magnetic field inhomogeneities of the MR scanner. To account for these acquisition-specific intensity ranges of edematous vs. non-edematous bone marrow, fuzzy C-means clustering [29,30] was applied to the intensity values of all voxels in each image, assuming two clusters. This yields two probability map images (one per cluster) where each voxel contains the probability of that voxel belonging to the respective cluster. Let C2 be the cluster whose center value is the higher of the two computed cluster centers. As Figure 2 illustrates, high probabilities (bright voxels) within the C2 probability map correspond to locations of high fluid content, such as BME and synovium.

For each carpal bone, the fraction of bone affected by BME was estimated as the fraction of voxels (out of the total number of voxels within the bone's segmentation) whose probability of belonging to C2 was higher than the threshold value T_{C2} (numeric value optimized below). The resulting quantitative BME measurement (BME-QM) takes any fractional values between 0 and 1.

Optimization

In order to optimize the T_{C2} threshold parameter based on correlation with visual BME scores, a training set of patients was defined. The number of patients with low-moderate BME in our cohort is much larger than the number of patients with severe BME. Therefore, random sampling of the cohort does not guarantee inclusion of patients with severe BME in the population sample. To ensure that patients with high degree of BME were represented in the training set, we categorized a set of 468 patients by the maximum visual BME score (R_{max}) across the carpal bones. Four sampling categories were defined corresponding to four intervals within R_{max} range. Table 1 lists the defined categories and the number of patients that fall into each category. Next, 15 patients were randomly selected from each category to form a training set of 60 patients.

Table 1. Training set sampling categories

Patient category index	R_{max} interval	Number of patients
0	$R_{max} = 0$	189
1	$0 < R_{max} \leq 1$	208
2	$1 < R_{max} \leq 2$	42
3	$2 < R_{max} \leq 3$	29

Note: Random sampling across all categories would form a training set that mainly consists of patients with $R_{max} \leq 1$. In contrast, randomly selecting 15 patients from category 3, for example, guarantees that the training set will include 15 patients in which at least one bone received a visual BME score greater than 2. Thus, random sampling from individual categories helps ensure T_{C2} is optimized with respect to the entire range of the visual BME score.
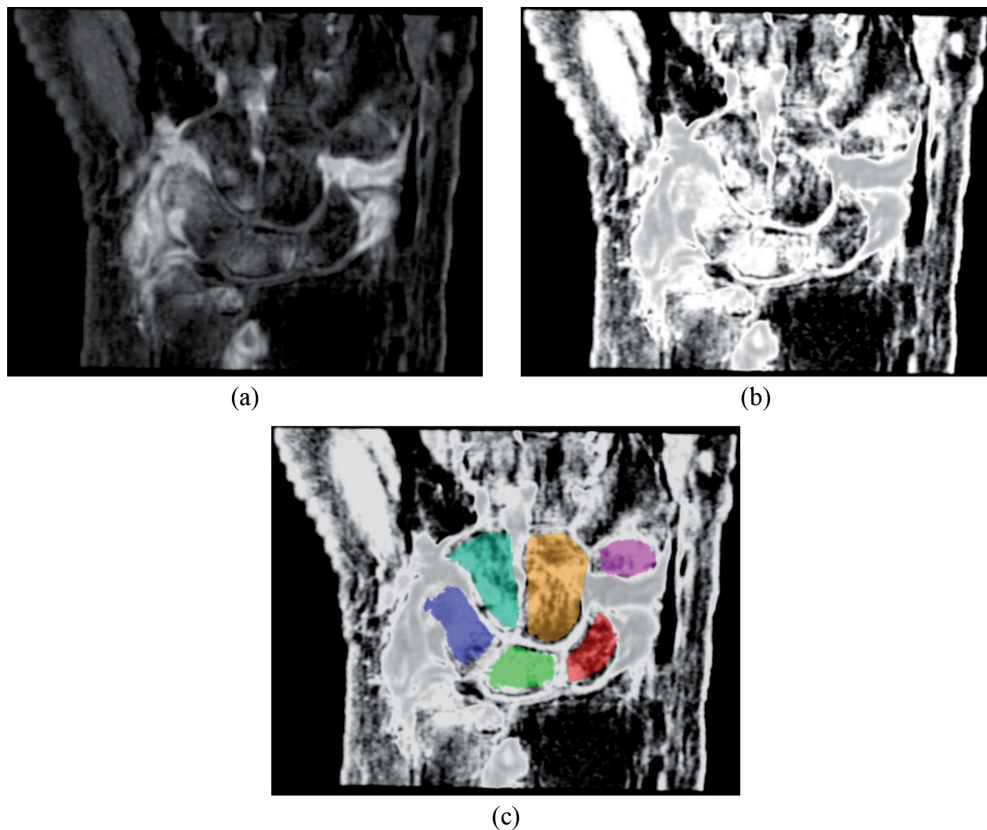

(a)

(b)

(c)

Figure 2. SRR image of the wrist (a), its C2 probability map image (b), and C2 image with carpal bone segmentation overlay from ABS (c).

To minimize the influence of acquisition artifacts and segmentation errors on threshold optimization, three patients whose MR scans suffered from incomplete fat suppression and one patient for which ABS failed were excluded from the obtained training set. This brought the final training set size to 56 patients. The optimal value of T_{C2} was found by maximizing the Pearson correlation coefficient r between the sum of visual BME scores across all carpal bones and the sum of BME-QM across all carpal bones.

Validation

After optimizing and locking the value of T_{C2}, the method was validated on 502 patients that were not part of the training set.

Statistical analysis

The Pearson correlation coefficient r between the sum of visual BME scores across all carpal bones and the sum of BME-QM across all carpal bones was evaluated. *P*-values below 0.05 were indicative of statistical significance. MR scans that suffered from incomplete fat suppression were noted and excluded from the correlation computation. Scans with other acquisition artifacts, such as noise patterns and incomplete field of view were excluded from the analysis. Patients in which one or more bones were not segmented by ABS yielded undefined values for BME-QM. Since undefined values cannot be included in the correlation computation, these patients were excluded from statistical analysis. The statistics were computed using MATLAB R2015b (MathWorks, Inc.).

Results

Assessment of segmentation accuracy

The mean bone-level recall and precision rates of ABS with respect to manual segmentations across 13 patients are shown in Figure 3. Recall rates were lowest in the pisiform (mean of 0.58 ± 0.09 SD) and highest in the capitate (mean of 0.82 ± 0.03 SD). Precision rates were high in all bones, with mean values ranging from 0.92 to 0.96 and SD values ranging from 0.02 to 0.05.
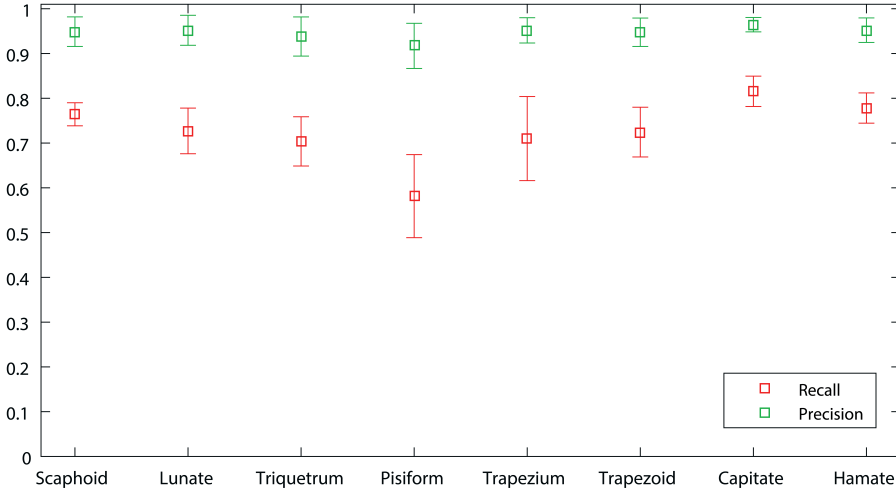
Figure 3. Mean (± SD) bone-level recall and precision rates of ABS with respect to manual segmentations across 13 patients.

Optimization

The maximum Pearson correlation ($r = 0.86$, $P < 0.001$), over 56 training set patients, between the sum of visual BME scores across all carpal bones and the sum of BME-QM across all carpal bones was achieved at threshold value $T_{C2} = 0.83$ (Figure 4). The scatter plot of the data is shown in Figure 5.

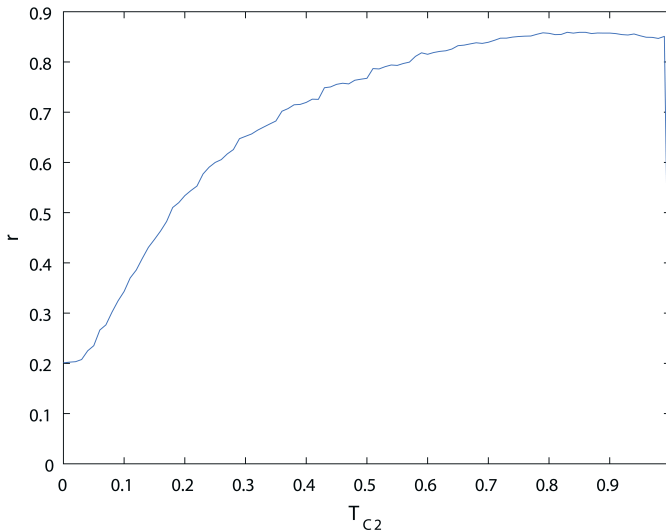
Figure 4. Pearson correlation coefficient r, over 56 training set patients, between the sum of visual BME scores across all carpal bones and the sum of BME-QM across all carpal bones, as a function of T_{C2}.
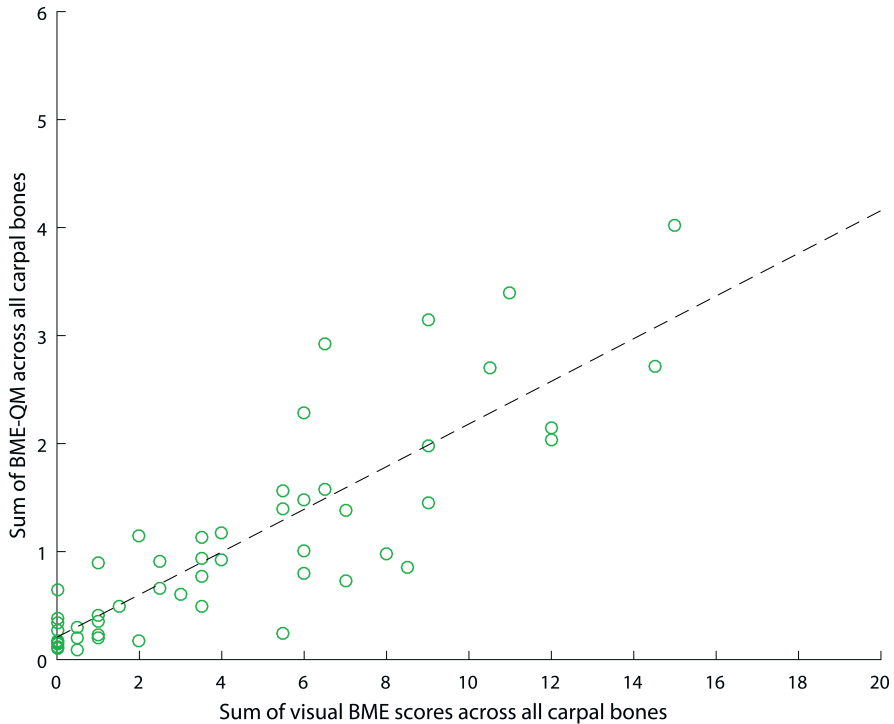
Figure 5. Scatter plot of sum of BME-QM across all carpal bones vs. sum of visual BME scores across all carpal bones for 56 training set patients. Each data point represents a single patient. $r = 0.86$, $P < 0.001$, $T_{C2} = 0.83$. Dashed black line represents linear regression fit.

Validation

Out of 502 patients, BME-QM was undefined in six patients due to failed segmentation. Three patients were excluded due to noise artifacts ($n = 2$) and incomplete field of view ($n = 1$) in their images. MR scans of eight patients suffered from incomplete fat suppression. For the remaining 485 patients, the Pearson correlation between the sum of visual BME scores across all carpal bones and the sum of BME-QM across all carpal bones was $r = 0.83$, $P < 0.001$. The scatter plot of the data is shown in Figure 6. Most patients formed clusters of steadily increasing BME-QM values, as the visual score value increased. Some outliers from this general trend were clearly visible for visual score value of 0 and BME-QM values between 1 and 2. These high quantitative values were due to

inaccurate segmentation of the carpal bones. Several patients whose images suffered from incomplete fat suppression produced BME-QM values that were largely deviating from the observed regression fit.
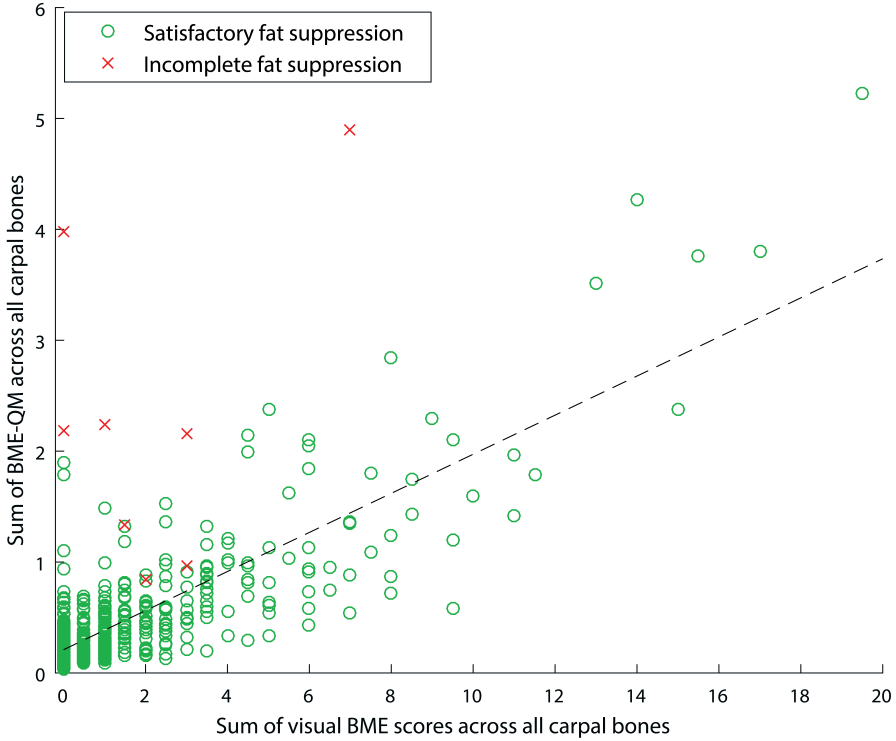

Figure 6. Scatter plot of sum of BME-QM across all carpal bones vs. sum of visual BME scores across all carpal bones for 493 validation set patients. Each data point represents a single patient. Linear regression fit (dashed black line) and Pearson correlation r were computed over 485 patients whose MR scans did not suffer from incomplete fat suppression (circular data points): $r = 0.83$, $P < 0.001$, $T_{C2} = 0.83$.

Discussion

In this study, we investigated the feasibility of automatic quantification of BME on MRI of the wrist in patients with early arthritis through an atlas-based approach. We chose to focus on the carpal bones, since they provide a complex multi-object scenario for exploring the feasibility of an atlas-based quantification framework. The advantage of this framework is that it can be straightforwardly expanded to other areas of the wrist and other joints by adding these areas of interest to the atlas. Validation results across 485 early arthritis patients indicated good

correlation between BME-QM and visual BME scores. It should be noted that perfect correlation is inherently not achievable because of the coarse grading scale of the visual score and the fine grading scale of BME-QM.

Our training strategy helped ensure that during validation BME-QM correlated well across the entire range of the visual BME score. The fact that the correlation curve in Figure 4 is relatively flat for T_{C2} values between 0.75 and 0.9 suggests that there is a range of T_{C2} values in this interval that result in good agreement between quantitative and visual scores. Furthermore, since BME-QM measures the fraction of voxels with C2 probability above T_{C2}, this seems to indicate that locations considered as BME in visual scoring often result in C2 probability values around 0.9. We also examined the effect of a smaller training set on T_{C2} optimization (data not shown), with five patients randomly selected from each R_{max} category forming a training set of 20 patients. We observed a similarly stable high correlation for T_{C2} values between 0.75 and 0.9, suggesting that the optimization step is not overly sensitive to training set size, as long as patients from all categories of BME severity (R_{max}) are represented in the training data.

The time required to execute the BME-QM framework for one patient on an Intel® Xeon® E5-1620 v3 CPU was ~58 min (SRR, ~20 min; ABS, ~35 min; BME quantification ~3 min). ABS is the most time-consuming step, but it can be accelerated 10-fold by running image registrations between all atlas images and the target image in parallel. Since registrations are independent of each other, this can be easily achieved given sufficient computing power. However, in large cohort studies, where evaluation of image data is often carried out days or weeks after the image is acquired, such acceleration may be irrelevant; an automatic framework can be executed immediately after image acquisition in an integrated fashion, thus ensuring quantitative results are available by the time a research project enters the evaluation phase.

ABS provided satisfactory segmentation for the vast majority of patients. In practice, failed segmentation cases will require manual adjustment by an expert in order for BME-QM to be computed. Over-segmentation of bones or shifted

segmentations that include synovium voxels increase the value of BME-QM due to contrast enhancement in the synovium. It is preferable to slightly under-segment the bone to ensure the exclusion of synovium while retaining most of the bone marrow within the segmentation. That said, significant under-segmentation may lead to an upward bias in BME-QM. Quantitative assessment of ABS accuracy in 13 patients revealed the tendency of ABS to under-segment bones (mid-range recall rates and high precision rates). Therefore, the current framework may raise false alarms when bone volume is under-estimated in the presence of moderate BME. The mid-range recall rates also suggest unwanted variability in BME-QM due to incomplete bone segmentation. The fact that the lowest recall rates were observed in the pisiform while the highest in the capitate, is likely due to the fact that the pisiform is the smallest of the carpal bones while the capitate is the largest of the carpal bones. An additional challenge during registration is the varied intensity and pattern of BME across patients. It is therefore advisable to avoid using very fine grid spacing during the B-spline registration step, since alignment between images on a coarser scale should be less sensitive to these local variations. Another potential pitfall is inclusion of erosions in the segmentation result. Erosions may contain high intensities that will mistakenly contribute to the value of BME-QM. To address these possible pitfalls and improve bone-level recall rates, an automatic refinement step should follow ABS in the future. In addition, to ensure robustness of the atlas to variations in MRI acquisition protocols and scanners at different sites, it may be necessary to form a larger atlas set consisting of sub-atlases of wrist scans acquired under different echo/repetition times and magnetic field strengths. The most suitable sub-atlas can then be automatically identified based on the acquisition parameters of a specific target image.

Incomplete fat suppression during acquisition of MR scans has an adverse effect on the accuracy of BME-QM. Bone marrow fat signal that is not properly suppressed results in high intensities that are mistaken for edema voxels by the clustering algorithm. Fat suppression quality requirements for BME-QM are higher compared to visual scoring. This is due to the availability of pre-contrast image

data in visual scoring and pattern recognition during visual assessment of increased signal intensity secondary to insufficient fat suppression. Although fat suppression issues are relatively rare, they must be identified prior to applying BME-QM to reduce false positives. The possibility of identifying and compensating fat suppression issues automatically should be investigated. In addition, more robust fat suppression techniques that are less sensitive to bulk susceptibility, such as Dixon techniques, may be beneficial when BME-QM is used.

A limitation of the current study is that the quality of carpal bone segmentation in training and validation set patients was judged subjectively. Quantitative assessment of segmentation accuracy was not possible, since no ground truth, manual segmentations were available for these patients. Quantification of segmentation accuracy would allow to supplement the BME measurement with a confidence measure. Another limitation is that pre-contrast image data could not be included in the framework, since pre-contrast T1 scans were acquired only in the coronal plane, while SRR requires a coronal and axial scan of the same sequence as input. Therefore, a straightforward voxel-to-voxel comparison between SRR T1-Gd images and pre-contrast T1 images was not possible. Inclusion of pre-contrast data would allow to explore a subtraction methodology as means of quantifying BME and could also facilitate the detection of fat suppression issues.

Recently, another framework aimed at automatically quantifying RA-related biomarkers, called quantitative RAMRIS (RAMRIQ), was proposed by Bowes *et al.* [31,32] and employed in a treatment effects study by Conaghan *et al.* [33]. These studies focus on measuring change over time, demonstrating higher sensitivity of quantitative measurements compared to RAMRIS. In contrast, we focused on validation of quantitative measurements at a single time point. In the future, it would be interesting to employ BME-QM for measuring change over time and evaluate its sensitivity.

Conclusion

We conclude that BME-QM has potential to provide a feasible alternative to visual scoring of BME on MRI of the wrist in patients with early arthritis. Complete automation requires further refinement of carpal bone segmentation and automatic detection and compensation of acquisition artifacts. Future work should also add more locations of interest relevant to RA to the atlas and extend this framework to other types of inflammation, such as synovitis and tenosynovitis. These developments can save time and manual effort for clinical researchers and help assess the value of MRI both for diagnosing RA and monitoring its treatment.

Acknowledgements

REFERENCES

1. McQueen FM, Benton N, Perry D, Crabbe J, Robinson E, Yeoman S, et al. Bone edema scored on magnetic resonance imaging scans of the dominant carpus at presentation predicts radiographic joint damage of the hands and feet six years later in patients with rheumatoid arthritis. Arthritis Rheum. 2003;48:1814–27.

2. Hetland ML, Ejbjerg B, Hørslev-Petersen K, Jacobsen S, Vestergaard A, Jurik AG, et al. MRI bone oedema is the strongest predictor of subsequent radiographic progression in early rheumatoid arthritis. Results from a 2-year randomised controlled trial (CIMESTRA). Ann. Rheum. Dis. 2009;68:384–90.

3. Bøyesen P, Haavardsholm EA, Ostergaard M, van der Heijde D, Sesseng S, Kvien TK. MRI in early rheumatoid arthritis: synovitis and bone marrow oedema are independent predictors of subsequent radiographic progression. Ann. Rheum. Dis. 2011;70:428–33.

4. Nieuwenhuis WP, van Steenbergen HW, Stomp W, Stijnen T, Huizinga TWJ, Bloem JL, et al. The Course of Bone Marrow Edema in Early Undifferentiated Arthritis and Rheumatoid Arthritis: A Longitudinal Magnetic Resonance Imaging Study at Bone Level. Arthritis Rheumatol. (Hoboken, N.J.). 2016;68:1080–8.

5. Østergaard M, Peterfy C, Conaghan P, McQueen F, Bird P, Ejbjerg B, et al. OMERACT Rheumatoid Arthritis Magnetic Resonance Imaging Studies. Core set of MRI acquisitions, joint pathology definitions, and the OMERACT RA-MRI scoring system. J. Rheumatol. 2003;30:1385–6.

6. Østergaard M, Edmonds J, McQueen F, Peterfy C, Lassere M, Ejbjerg B, et al. An introduction to the EULAR-OMERACT rheumatoid arthritis MRI reference image atlas. Ann. Rheum. Dis. 2005;64:i3-7.

7. Diamond AL. Foveal simultaneous brightness contrast as a function of inducing, and test-field luminances. J. Exp. Psychol. 1953;45:304–14.

8. Heinemann EG. Simultaneous brightness induction as a function of inducing- and test-field luminances. J. Exp. Psychol. 1955;50:89–96.

9. Leibowitz H, Mote FA, Thurlow WR. Simultaneous contrast as a function of separation between test and inducing fields. J. Exp. Psychol. 1953;46:453–6.

10. Li X, Yu A, Virayavanich W, Noworolski SM, Link TM, Imboden J. Quantitative characterization of bone marrow edema pattern in rheumatoid arthritis using 3 Tesla MRI. J. Magn. Reson. Imaging. 2012;35:211–7.

11. Teruel JR, Burghardt AJ, Rivoire J, Srikhum W, Noworolski SM, Link TM, et al. Bone

structure and perfusion quantification of bone marrow edema pattern in the wrist of patients with rheumatoid arthritis: a multimodality study. J. Rheumatol. 2014;41:1766–73.

12. Yang H, Rivoire J, Hoppe M, Srikhum W, Imboden J, Link TM, et al. Computer-aided and manual quantifications of MRI synovitis, bone marrow edema-like lesions, erosion and cartilage loss in rheumatoid arthritis of the wrist. Skeletal Radiol. 2015;44:539–47.

13. Li X, Ma BC, Bolbos RI, Stahl R, Lozano J, Zuo J, et al. Quantitative assessment of bone marrow edema-like lesion and overlying cartilage in knees with osteoarthritis and anterior cruciate ligament tear using MR imaging and spectroscopic imaging at 3 Tesla. J. Magn. Reson. Imaging. 2008;28:453–61.

14. Dodin P, Abram F, Pelletier J-P, Martel-Pelletier J. A fully automated system for quantification of knee bone marrow lesions using MRI and the osteoarthritis initiative cohort. J. Biomed. Graph. Comput. 2012;3:51.

15. Dodin P, Martel-Pelletier J, Pelletier J-P, Abram F. A fully automated human knee 3D MRI bone segmentation using the ray casting technique. Med. Biol. Eng. Comput. 2011;49:1413–24.

16. de Rooy DPC, van der Linden MPM, Knevel R, Huizinga TWJ, van der Helm-van Mil AHM. Predicting arthritis outcomes--what can be learned from the Leiden Early Arthritis Clinic? Rheumatology (Oxford). 2011;50:93–100.

17. Stomp W, Krabben A, van der Heijde D, Huizinga TWJ, Bloem JL, van der Helm-van Mil AHM, et al. Aiming for a shorter rheumatoid arthritis MRI protocol: can contrast-enhanced MRI replace T2 for the detection of bone marrow oedema? Eur. Radiol. 2014;24:2614–22.

18. Sudoł-Szopińska I, Jurik AG, Eshed I, Lennart J, Grainger A, Østergaard M, et al. Recommendations of the ESSR Arthritis Subcommittee for the Use of Magnetic Resonance Imaging in Musculoskeletal Rheumatic Diseases. Semin. Musculoskelet. Radiol. 2015;19:396–411.

19. Frenzel T, Apte C, Jost G, Schöckel L, Lohrke J, Pietsch H. Quantification and Assessment of the Chemical Form of Residual Gadolinium in the Brain After Repeated Administration of Gadolinium-Based Contrast Agents. Invest. Radiol. 2017;1–9.

20. Radbruch A, Haase R, Kickingereder P, Bäumer P, Bickelhaupt S, Paech D, et al. Pediatric Brain: No Increased Signal Intensity in the Dentate Nucleus on Unenhanced T1-weighted MR Images after Consecutive Exposure to a Macrocyclic Gadolinium-based Contrast Agent. Radiology. Radiological Society of North America; 2017;1–9.

21. Greenspan H, Oz G, Kiryati N, Peled S. MRI inter-slice reconstruction using super-resolution. Magn. Reson. Imaging. 2002;20:437–46.

22. Shilling RZ, Robbie TQ, Bailloeul T, Mewes K, Mersereau RM, Brummer ME. A super-resolution framework for 3-D high-resolution and high-contrast imaging using 2-D multislice MRI. IEEE Trans. Med. Imaging. 2009;28:633–44.

23. Woo J, Murano EZ, Stone M, Prince JL. Reconstruction of high-resolution tongue volumes from MRI. IEEE Trans. Biomed. Eng. 2012;59:3511–24.

24. Poot DHJ, Van Meir V, Sijbers J. General and efficient super-resolution method for multi-slice MRI. Med. Image Comput. Comput. Assist. Interv. 2010;13:615–22.

25. Klein S, Staring M, Murphy K, Viergever MA, Pluim JPW. elastix: a toolbox for intensity-based medical image registration. IEEE Trans. Med. Imaging. 2010;29:196–205.

26. Aizenberg E. Elastix parameters for alignment between coronal and axial images of the wrist [Internet]. 2016. Available from: http://elastix.bigr.nl/wiki/index.php/Par0040

27. Rohlfing T, Brandt R, Menzel R, Russakoff DB, Maurer CRJ. Quo vadis, atlas-based segmentation? Handb. Med. Image Anal. - Vol. III Regist. Model. 2005. p. 435–486.

28. Aizenberg E. Elastix parameters for atlas-based segmentation of carpal bones [Internet]. 2016. Available from: http://elastix.bigr.nl/wiki/index.php/Par0041

29. Bezdek JC. Pattern Recognition with Fuzzy Objective Function Algorithms. Kluwer Academic Publishers; 1981;

30. Amiri M. Yashil's Fuzzy C-Means Clustering MATLAB Toolbox Ver. 1.0 [Internet]. 2003. Available from: http://ce.sharif.edu/~m_amiri/project/yfcmc/index.htm

31. Bowes MA, Guillard G, Gill E, Vincent GR, Hensor E, Freeston JE, et al. Novel Quantification of MRI Provides a More Sensitive Outcome Measure Than RAMRIS. 2014 ACR/ARHP Annu. Meet. 2014.

32. Bowes MA, Guillard G, Vincent GR, Freeston JE, Vital EM, Emery P, et al. Quantitative MRI Measurement of Tenosynovitis Demonstrates Differing Responses of Synovitis and Tenosynovitis after RA Treatment. 2015 ACR/ARHP Annu. Meet. 2015.

33. Conaghan PG, Østergaard M, Bowes MA, Wu C, Fuerst T, van der Heijde D, et al. Comparing the effects of tofacitinib, methotrexate and the combination, on bone marrow oedema, synovitis and bone erosion in methotrexate-naive, early active rheumatoid arthritis: results of an exploratory randomised MRI study incorporating semiquantitati. Ann. Rheum. Dis. 2016;